IEEE Access
Multidisciplinary | Rapid Review | Open Access Journal

Received 15 August 2022, accepted 19 August 2022, date of publication 26 August 2022, date of current version 2 September 2022.

Digital Object Identifier 10.1109/ACCESS.2022.3202197

RESEARCH ARTICLE

A Deep-Learning-Based Optimal Energy Flow Method for Reliability Assessment of Integrated Energy Systems

ZIHENG DONG, KAI HOU, (Member, IEEE), ZEYU LIU, (Student Member, IEEE), XIAODAN YU, HONGJIE JIA, (Senior Member, IEEE), AND QIAN XIAO, (Member, IEEE)
Key Laboratory of Smart Grid of Ministry of Education, Tianjin University, Tianjin 300072, China
Corresponding author: Zeyu Liu (tjulzy@tju.edu.cn)

This work was supported by the National Natural Science Foundation of China under Grant 52077150/U2066213.

ABSTRACT The energy interactions and uncertain factors of integrated energy systems (IES) have brought risks to the reliable energy supply. A large number of states need to be analyzed to obtain a stable reliability value. However, different operating characteristics complicate the optimal energy flow (OEF) model, which brings tremendous computational cost. To address that, a deep-learning-based approach is proposed as an alternative way to solve the OEF problems. This approach constructs the mapping between system state and energy allocation to directly obtain the optimal load curtailment. Thereafter, the deep-learning-based reliability assessment framework for IES is proposed to improve efficiency. Additionally, the Gaussian noise and data-processing strategies are involved to achieve higher accuracy. Compared to the model-based approach, the proposed method increases the reliability assessment efficiency by 6 orders of time. With an accuracy of over 95%, it outperforms other autoencoder and random forest methods. Method accuracy has remained above 90% in various scenarios.

INDEX TERMS Integrated energy system, deep learning, optimal energy flow, stacked denoising auto-encoder (SDAE), reliability assessment.

I. INTRODUCTION

Integrated energy system (IES) has shown a promising landscape for its characteristics in energy sharing and flexible energy management [1]. However, the interconnection of energy can trigger unexpected failures and deteriorate the reliability of the energy supply. The blackout of Texas in 2021 can be traced to the gas blockage [2], [3]. A similar reason accounts for the blackouts that occurred in Singapore and England [4]. Reliability assessment of IES reflects the supplying reliability of IES and can be used as a quantitative analysis tool [5] for upgrading and planning. Therefore, the issue of IES reliability has become more critical.

Reliability assessment can qualitatively or quantitatively assess the potential risks from various uncertainties in the integrated energy system [5]. Accurate modeling for energy interaction is crucial in the quantitative analysis of IES reliability assessment. Compared with the traditional power system, bidirectional energy interactions and physical characteristics should be studied to evaluate the reliability level [6], [7]. Residual gas [8] and the dynamic transmission process [9] are incorporated into the reliability assessment process. Some byproducts of gas utilization, including smoke and steam, are considered to refine the fluid model [10]. Multi-energy flow model of the power and heat system is decoupled to accelerate the calculation [11]. Moreover, IES reliability is also influenced by the uncertainties of renewable energy installation and multiple types of loads [12].

Optimal energy flow can be used to calculate the optimal load curtailment after the equipment failure in reliability assessment [13]. By analogy with the optimal power flow [14], OEF is also used to optimize the generation dispatch or minimize the energy shedding under a particular objective function. For formulating the interactions of IES,

The associate editor coordinating the review of this manuscript and approving it for publication was R. K. Saket.

OEF is an effective tool to address the scheduling problem across multiple energy systems and optimize energy distribution [13]. The OEF is applied to optimize the energy utilization of IES considering the carbon emission [15] and economical factors [16]. A two-stage stochastic programming model is presented to evaluate the operational risk of IES with high penetration of renewable energy [14]. Considering a set of economic factors, a hybrid energy sharing framework is applied to a heat-electricity system [15]. A day-ahead energy trading strategy is proposed to reach a win-win situation of efficient utilization and economic operation [16]. Apart from the diversity of optimization goals, the optimization and analysis can be realized in a variety of ways, such as the contract theory and game model. The former can be used in a closed-loop energy coordinative framework [17], and a Stackelberg game model is used to coordinate multi-energy flow [18]. In summary, the researchers mainly endeavor to improve the OEF accuracy, but the model complexity brings a heavy computation burden. In each system state, minimum load curtailment needs to be determined, and repetitive OEF solving is also time-consuming [19].

As a new-arising technology, deep-learning approaches bypass the physical model to solve complex OEF problems. A deep learning approach is applied to manage the cooling/heating energy of the building [20]. And the energy optimization can be further improved with load demand forecasting in a deep learning way [21], [22]. With the Industrial Internet of Things (IIoT) gaining more importance in modern industry, an IIoT-based framework is combined with deep reinforcement learning techniques to optimize energy utilization [15]. Allowing uncertainties, a random-forest-based method is devised to optimize the distribution of power and gas [23], [24]. Although the deep learning approaches have shown high efficiency, a comprehensive method based on Monte Carlo simulation and the energy flow model is commonly used in existing IES reliability works [25], [26]. However, studies of the deep learning applications in the IES reliability assessment are relatively rare. Further research is still needed.

In this paper, a deep-learning method is proposed to solve the OEF in a faster manner for reliability assessment. First, a stacked denoising auto-encoder (SDAE) is developed to map the relationship between the system state and optimal operational results. Thereafter, the SDAE-based network is used to determine the load curtailment of system states considering the multiple uncertainties. The reliability indices are calculated based on the load curtailment and the weakness of IES can be identified in terms of energy shortage. In summary, the main contributions are as follows,

- A deep-learning approach based on an SDAE network is proposed to determine the optimal energy flow in IES with high efficiency and acceptable accuracy. This technique is an alternative way to the traditional model-based optimization algorithms. It can approximate the relationship between system states and optimal results.
- A novel deep-learning-based reliability assessment framework is developed for IESs. Applying deep-learning OEF to reliability assessment contributes to the analysis of large numbers of system states in batches and significantly improves the efficiency of reliability assessment.
- Considering the data characteristics of OEF, the Gaussian noise and data-filtering strategy are proposed to improve the accuracy of results.

The remaining paper is organized as follows. The SDAE network is introduced in section II. In Section III, the challenges in IES reliability assessment are discussed and a deep-learning framework is proposed. Section IV presents the SDAE-based OEF learning process, including the network design and network training. The overall procedure is described in section V. Numerical results with the proposed method are shown in section VI. Finally, the paper is concluded in section VII.

II. INTRODUCTION OF SDAE NETWORK

This section briefly introduces the autoencoder (AE) and relevant variants, including denoising autoencoder (DAE) and stacked denoising autoencoder (SDAE).

1) AUTOENCODER

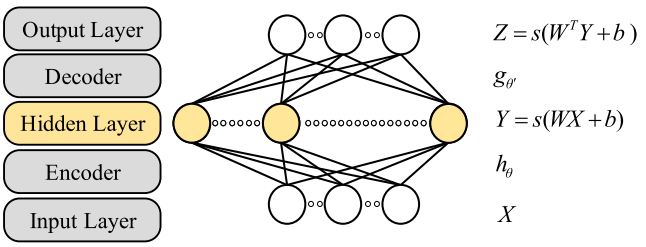

FIGURE 1. The structure of the Autoencoder.

Autoencoder is a feedforward network with a single hidden layer. The encoded feature output by the hidden layer can be expressed as,

$$h(x_i) = s(Wx_i + b) \tag{1}$$

where $s(')$ denotes the activation function. h is the encoding transforming function. x_i is the input vector of the ith sample. W and b represent weights and bias in the hidden layer, respectively. Then the hidden layer output matrix can be obtained by gathering $h(x_i)$ of all samples.

$$Y = \left[h(x_1), h(x_2), \cdots, h\left(x_{N_S}\right)\right] = s(WX + b) \tag{2}$$

where Y is the encoding feature. N_s is the sample number. The hidden layer output is the encoding form of the input features.

The key idea of AE is to write the original input features while keeping valuable features in the encoding form. Decoding can be used to test whether valuable features are kept. If the feature can be decoded into the original form, Y contains the valuable information of the original input. The feature reconstruction in the decoder can be expressed as,

$$Z = g(Y) = s\left(W^T Y + b'\right) \tag{3}$$

where Z is the decoding output. $g(Y)$ denotes the decoding transforming function. W^T and b' represent weights and bias in the decoding layer. Therefore, the size of Z is the same as that of the original input X.

2) DENOISING AUTOENCODER

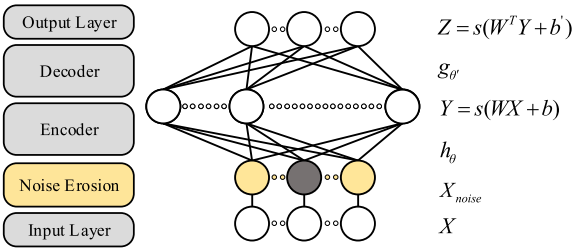

FIGURE 2. The structure of denoising autoencoder.

Denoising autoencoder is the network with a noise erosion layer at the front of AE. The noise erosion layer is used to add noise to the input so the network can be trained against noise. By training the network with additional noise, DAE can obtain a denoising effect. A practical way of noise erosion is the "random mask", i.e., randomly setting the original value to zero. The erosion can be expressed as,

$$X_{noise} = sgn\,(r - p)\,X \tag{4}$$

where X_{noise} is the input with noise erosion. sgn(r-p) is the signal function. r is a random number. p is the probability of erosion.

3) STACKED DENOISING AUTOENCODER

The difference between the traditional AE and the SDAE-based network is the stacked structure and the noise erosion layer. The stacked structure brings more nonlinear transformations to solve the linear-inseparable problem.

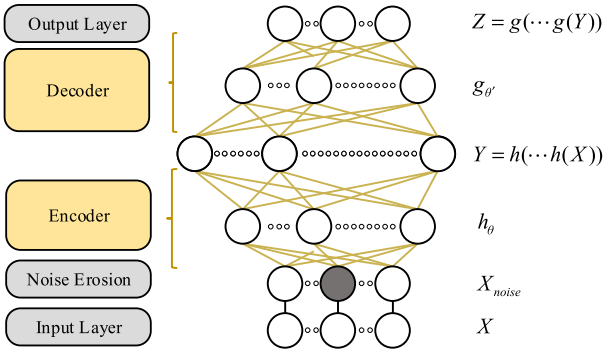

FIGURE 3. The structure of stacked denoising autoencoder.

The stacked structure can process the input data in a chain of linear-nonlinear transformations [27]. The chain operation eventually extracts abstract features and rebuilds original features. The encoding and decoding process can be expressed as (5) and (6), respectively.

$$Y_l = h^l\left(h^{l-1}\left(h^{l-2}\left(\cdots h^1\left(X_{noise}\right)\right)\right)\right) \tag{5}$$

$$Z_l = g^l\left(g^{l-1}\left(g^{l-2}\left(\cdots g^1\left(Y_l\right)\right)\right)\right) \tag{6}$$

where Y_l and Z_l are the outputs of the lth encoder and decoder layer, respectively.

III. PROBLEM STATEMENT AND SOLUTION FRAMEWORK

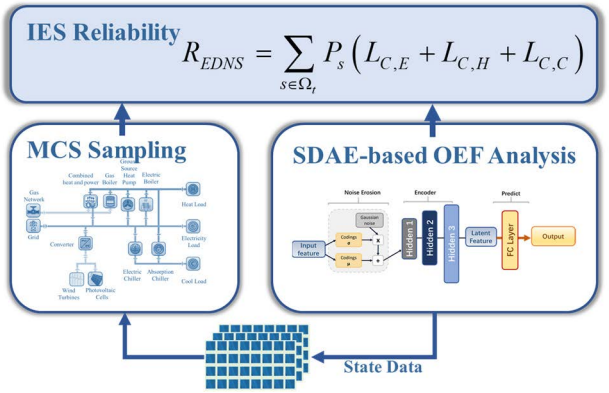

FIGURE 4. The deep-learning framework of reliability assessment.

The reliability assessment is to evaluate the reliability levels of the possible scenarios based on their probabilities and impacts. The probability of the system state is obtained from the out-of-service probability of the equipment, while the impact is determined by solving the OEF in IES. In the reliability assessment, all the uncertainties should be analyzed to calculate the optimal load curtailment.

The deep learning method is a model-free way to calculate the optimal load curtailment by mapping the relationship with weight matrices and bias vectors. This method is the matrix calculation which is easy to extend for batch calculations. Therefore, it can accelerate the analysis of OEF for massive system states. To this end, a data-driven approach to solving OEF is the core of the reliability assessment scheme for IES.

The proposed deep-learning IES reliability framework is shown in Fig.4. The probability is based on Monte-Carlo Simulation, while the impact is calculated via the SDAE-based OEF learning approach. The proposed framework includes three stages.

Stage 1: IES state sampling. The possible system states are selected based on the Monte-Carlo simulation and equipment failure model.

Stage 2: SDAE-based OEF analysis. The selected states are analyzed and the optimal energy curtailment is determined based on the proposed deep-learning-based OEF.

Stage 3: IES reliability index. The reliability is calculated in terms of the expected demand not supplied (EDNS). The reliability index is expressed in a weighted form where state probabilities are regarded as the weights.

A. SELECT STATES VIA MCS

The MCS method relies on repeated random samplings to estimate reliability indices. Equipment samples are obtained

by MCS and the two-state model can be expressed as,

$$s_k = \begin{cases} 0, & if\ r > U_k \\ 1, & else \end{cases} \tag{7}$$

where s_k is the kth equipment state. r is a random value. U_k is the out-of-service probability of the kth equipment. The system states are determined by combining all the equipment states, which can be expressed as,

$$s_{IES} = \left(\bigcup_{k \in \Omega_{IES}} s_k C_k \right) \cup \varphi \cup v \tag{8}$$

where s_{IES} is the system state of IES, which is represented by the capability of available equipment and the current wind speed and solar irradiation. Ω_{IES} is the set of equipment states. C_k is the capacity of kth equipement.

The weather factors are randomly chosen from the historical data. φ is the solar irradiation. v is the wind speed. For each particular system state, the state probability can be expressed as,

$$P_s = \frac{N_s}{N} \tag{9}$$

where P_s is the system state probability. N_s is the occurrence of system state s. N is the total number of system states.

B. STATE ANALYSIS AND OPTIMAL ENERGY FLOW

Energy interaction is supported by the energy converting equipment, including combined heat and power units (CHP), geothermal pump (GHP), gas boiler (GB), air source heat pump (ASHP), electric chiller (EC), absorption chiller (AC), etc. To address the bi-direction interaction, the OEF is developed to formulate the energy interaction and determine energy utilization. Renewable energies are plugged into the IES with a power conversion system (PCS). In the reliability assessment, the optimal energy flow aims to minimize the curtailment of load and renewable energy, and the objective function is expressed as,

$$f = w_1 L_{C,H} + w_2 L_{C,E} + w_3 L_{C,C} + w_4 (L_{C,Wt} + L_{C,Pv}) \tag{10}$$

where $L_{C,H}$, $L_{C,E}$, and $L_{C,C}$ are the load curtailment of heating, electricity, and cooling, respectively. $L_{C,Wt}$ is the wind energy curtailment. $L_{C,Pv}$ is the solar energy curtailment. w_i is the weight of the ith curtailment. The first three items are designed to meet the load demand as much as possible, while other items are used to maximize the utilization of renewable energy.

Equality constraints include energy balance constraints of each subnetwork.

$$\begin{aligned} &P_{Grid} + P_{Chp} + (P_{Wt} + P_{Pv}) f_{Pcs} \\ &\quad = L_{D,E} - L_{C,E} + P_{Ec} + P_{Ashp} + P_{Ghp} \end{aligned} \tag{11}$$

where P_{Grid} is the power purchased from the grid. P_{Chp} is the power output of CHP units. P_{Wt} and P_{Pv} are the power injection of the wind turbines and photovoltaic cells, respectively. f_{Pcs} is the efficiency factor of PCS. $L_{D,E}$ is the electricity load. P_{Ec}, P_{Ashp}, and P_{Ghp} are the power consumption of electric chiller, air source heat pump, and ground source heat pump, respectively.

$$P_{Pv} = P_{Pv,\max} - L_{C,Pv} \tag{12}$$

$$P_{Wt} = P_{Wt,\max} - L_{C,Wt} \tag{13}$$

where $P_{Wt,\max}$ and $P_{Pv,\max}$ are the available capacities of wind farm and the photovoltaic system, which can be obtained based on the wind speed and solar irradiation. The relationship can be expressed as,

$$P_{Wt,\max} = \begin{cases} 0 & v < v_{CI}, v > v_{CO} \\ P_{Wt}^R \dfrac{v - v_{CI}}{v_R - v_{CI}} & v_{CI} \le v \le v_R \\ P_{Wt}^R & v_R < v \le v_{CO} \end{cases} \tag{14}$$

where $PR\ Wt$ is the available and rated power output. v is the current wind speed. v_R, v_{CI}, and v_{CO} are the rate of wind speed, cut-in wind speed, and cut-out wind speed.

The photovoltaic generation is controlled by the maximum power point tracking (MPPT) technique. In MPPT control, the output of PV can be expressed as,

$$P_{Pv,\max} = \rho_{Pv} P_{Pv}^R \frac{\varphi}{\varphi_{STC}} \left[1 + \gamma \left(T_{Pv} - T_{Pv}^R \right) \right] \tag{15}$$

where $P_{Pv,\max}$ is the maximum power output of PV at the current time. φ_{STC} is the standard irradiation. T_{Pv} is the actual PV temperature. $TR\ Pv$ is the reference temperature. $PR\ Pv$ is the rated power output of the photovoltaic cells. ρ_{Pv} is an inner parameter. γ is an efficiency factor related to the temperature.

$$\begin{aligned} L_{D,H} - L_{C,H} + Q_{Ac} = {} & P_{Chp} f_{H2P,Chp} + f_{Ashp} P_{Ashp} \\ & + f_{Ghp} P_{Ghp} + Q_{Gb} \end{aligned} \tag{16}$$

where $L_{D,H}$ is the heat load. Q_{Ac} is the heat consumption of AC. P_{Chp} is the power output of CHP and $f_{H2P,Chp}$ is the heat-power ratio of energy conversion. f_{Ashp} is the ASHP conversion efficiency. f_{Ghp} is the GHP conversion efficiency. Q_{Gb} is the thermal generation of GB.

$$L_{D,C} - L_{C,C} = f_{Ec} P_{Ec} + f_{Ac} Q_{Ac} \tag{17}$$

where $L_{D,C}$ is the cool load. f_{Ec} is the efficiency factor of EC. f_{Ac} is the cool-heat ratio of AC.

Inequality constraints include operational limits in power, heating, and cooling systems.

$$\begin{cases} P_{Grid,\min} \le P_{Grid} \le P_{Grid,\max} \\ 0 \le P_{Chp} \le C_{Chp} \\ 0 \le Q_{Gb} \le C_{Gb} \\ 0 \le P_{Ec} \le C_{Ec} \\ 0 \le P_{Ashp} \le C_{Ashp} \\ 0 \le P_{Ghp} \le C_{Ghp} \\ 0 \le Q_{Ac} \le C_{Ac} \\ 0 \le P_{Wt} + P_{Pv} \le C_{pcs} \\ 0 \le P_{PV} \le C_{Pv} \\ 0 \le \varphi \le \varphi_{\max} \end{cases} \tag{18}$$

where $P_{Grid,\min}$ and $P_{Grid,\max}$ are the lower and upper limitations of electricity purchased from the grid. C denotes the equipment capability, for example, C_{pcs} is the capacity of the power conversion system.

C. RELIABILITY INDEX

The IES reliability can be evaluated with the expected value based on the probability of system state and the optimal load curtailment.

$$R_{EDNS} = \sum_{s \in s_{IES}} P_s \left(L_{C,E} + L_{C,H} + L_{C,C} \right) \tag{19}$$

where R_{EDNS} is the reliability index in terms of expected demand not supplied (EDNS). s is the system state. P_s is the possibility of the state s, which is calculated by (9). s_{IES} is the set of the possible system states in period time t, which is determined by MCS as (8). $L_{C,H}$, $L_{C,E}$, and $L_{C,C}$ are traditionally obtained by solving the equations (10)-(18), while they can be directly predicted by the SDAE network once it is trained. Section IV details this training process.

IV. SDAE-BASED OPTIMAL ENERGY FLOW APPROACH

A neural network with a particular structure can be considered as a function set, where different functions can be obtained by changing network parameters. In a supervised learning process, network parameters are learned through a gradient-descent process.

A. OPTIMAL ENERGY FLOW FEATURES

The optimal multi-energy flow contains the multi-energy features and their influence mechanism, including the capacity of the energy generation, energy conversion, and the internal physical laws. These multi-energy features, including optional factors and unchangeable variables, are closely dependent on each other and eventually influence the energy curtailment. From the OEF model, the dependence between the decision variables and other uncontrollable factors follows a function. From the perspective of deep learning, solving the OEF problem can be regarded as regression work. The relationship between the energy variables is mapped, whereby operating variables are predicted.

The curtailment of load and renewable energy are directly related to the equipment capacities, load demand, and actual power outputs of WT and PV. Since the other arguments in the physical model like constant efficiency factors remain unchanged, they can be excluded from input data. Therefore, the input vector $\boldsymbol{X}$ and the output vector $\boldsymbol{Y}$ are as follows,

$$\begin{aligned} \boldsymbol{X} = [&C_{Chp}, C_{Gb}, C_{Ec}, C_{Ashp}, C_{Ghp}, C_{Ac}, C_{cvt}, \\ &C_{PV}, P_{WT,\max}, P_{PV,\max}, L_{D,E}, L_{D,H}, L_{D,C}, v, \varphi] \end{aligned} \tag{20}$$

$$\begin{aligned} \boldsymbol{Y} = [&P_{Grid}, P_{CHP}, Q_{GB}, P_{Ashp}, P_{Ghp}, P_{Ec}, Q_{Ac}, \\ &P_{Wt}, P_{Pv}, L_{C,E}, L_{C,H}, L_{C,C}, L_{C,Wt}, L_{C,Pv}] \end{aligned} \tag{21}$$

B. PRE-TRAIN ENCODER: FEATURE EXTRACTION

In the pre-train stage, a large size of unlabelled data is used to outline the initial value of encoder parameters in an improved network with Gaussian noise erosion. The improved SDAE network is shown in Fig.5.

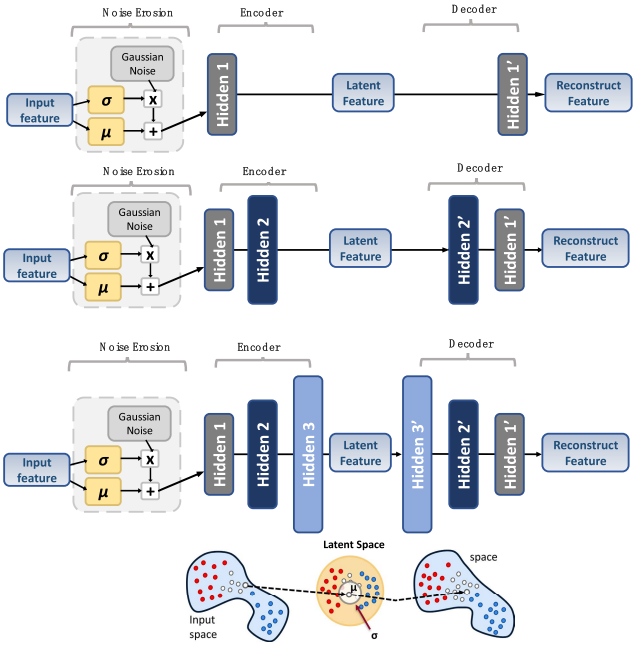

FIGURE 5. The proposed structure of the pre-train stage.

To increase the feature diversity and extract fine features, hidden layers should be larger with the depth increasing of the encoder. In the traditional structure, the size of the middle layer is the smallest to compress and filter features. However, the structure of the encoder is inverted in our network, allowing for rewriting features in a high-dimensional way.

The features are extracted and rewritten more abstractly in a high-dimensional way. Training with noise endows the network with anti-noise ability and robustness. In the classic SDAE network, the random mask strategy is widely used to add noise as equation (4). It is unsuitable for the state data of IES, which may block the key features out of the network. A random Gaussian noise strategy is expressed as,

$$X_{noise} = \eta X \odot sgn\left(r - p\right) + X \tag{22}$$

where X_{noise} is the input vector added with noise. η is the noise ratio, which obeys a Gaussian distribution. r is a random vector. p is the probability vector of noise arising. sgn(r - p) is the noise flag in the Monte-Carlo simulation. $\odot$ represents the element-wise multiplication. The randomly selected parts of data are added with Gaussian noise. This strategy prevents data distortion and increases sample diversity.

Feature extraction relies on the value of encoder parameters. However, direct learning parameters of all the encoder layers are intractable. To solve this problem, this pre-train stage is completed layer by layer in a symmetric network of encoder-decoder. For example, the first encode layer (Hidden 1 in Fig.5) is trained in the subnetwork Hidden1-Hidden1'. Then, each encoder layer and corresponding decoder layer are added to the subnetwork and the new layers are trained in the same way.

In each subnetwork, the encoder layers rewrite the input feature into a latent feature, and the large difference in the input variables can be mapped to the relative neighborhood in the latent space. The latent feature is decoded to its original form. A successful encode-decode process reflects the ability of feature extracting because the encoder keeps valuable features and rewrites them. To minimize the difference between reconstruction features and initial features, the loss function is designed as,

$$L_H(X, Z_l) = \|X - Z_l\|_2^2 \tag{23}$$

where L_H is the loss function in the pre-training stage, which is mainly for hidden layer updating. $||X - Z_l||_2$ is the Euclid norm of the residual vector. Z_l is the reconstruction feature of the lth DAE. The weights and biases are updated by the mini-batch gradient descent method in SDAE pre-training. The process can be expressed as,

$$\begin{cases} W_{ij}^{'(l,t+1)} = W_{ij}^{'(l,t)} - \eta\left(\frac{1}{n}\sum_{k=1}^{n}\frac{\partial L_H(X,Z_l)}{\partial W_{ij}^{'(l,t)}}\right) \\ \quad + \mu \times \Delta W_{ij}^{'(l,t-1)} \\ b_i^{'(l,t+1)} = b_i^{'(l,t)} - \eta\left(\frac{1}{n}\sum_{k=1}^{n}\frac{\partial L_H(X,Z_l)}{\partial b_i^{'(l,t)}}\right) \\ \quad + \mu \times \Delta b_i^{'(l,t-1)} \\ b_i^{(l,t+1)} = b_i^{(l,t)} - \eta\left(\frac{1}{n}\sum_{k=1}^{n}\frac{\partial L_H(X,Z_l)}{\partial b_i^{(l,t)}}\right) \\ \quad + \mu \times \Delta b_i^{(l,t-1)} \end{cases} \tag{24}$$

where η is the learning rate. μ is the momentum factor. n is the neuron number of the lth layer.

C. FINETUNE: OEF RELATIONSHIP MAPPING

In finetune stage, the deep network learns the OEF relationship in a supervised way. The process of supervised learning is finetuning all parameters based on the difference between the prediction and the actual value (i.e., label data). The prediction value is obtained from a deep auto-encoder network and a fully connected (FC) layer. The size of the original feature is expanded in our encoder, as shown in Fig.6.

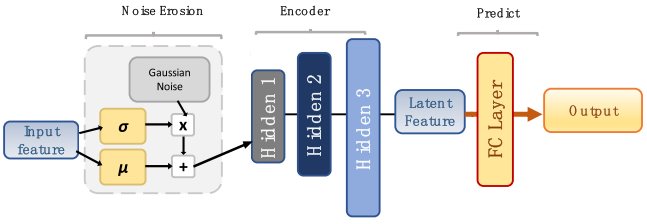

FIGURE 6. Deep network for OEF prediction.

The difference can be evaluated in the loss function,

$$L_F(\hat{Y}, Y_T) = \left\|\hat{Y} - Y_T\right\|_2^2 \tag{25}$$

where L_F denotes the loss function used in the finetune stage, which is mainly for FC layer updating. $\hat{Y}$ is the network prediction. Y_T is the actual value, which serves as the target output. $||\hat{Y} - Y_T||_2$ is the Euclid norm of the residual vector.

In the finetune stage, the pre-training results are used as the initial values of the encoder. Note that a smaller learning rate is selected to adjust network parameters, which is 1% of that in the pre-training stage. In this process, the gradient descent algorithm is adopted to minimize the gap between predictions and actual values. To speed up the training process, the whole dataset is separated into several batches. The updating rules based on the Adam optimizer in a single batch are shown as,

$$\omega_j^{\tau} = \omega_j^{\tau-1} - \frac{a \cdot \left(\frac{m_j^{\tau}}{1-\beta_1}\right)}{\sqrt{\frac{v_j^{\tau}}{1-\beta_2}} + \varepsilon} \tag{26}$$

$$m_j^{\tau} = \beta_1 m_j^{\tau-1} + (1-\beta_1)\frac{\partial L_F(\hat{Y}^{\tau-1}, Y_T)}{\partial \omega_j^{\tau-1}} \tag{27}$$

$$v_j^{\tau} = \beta_2 v_j^{\tau-1} + (1-\beta_2)\left(\frac{\partial L_F(\hat{Y}^{\tau-1}, Y_T)}{\partial \omega_j^{\tau-1}}\right)^2 \tag{28}$$

where a is the initial learning rate. ε is a very small value to avoid the denominator decreasing to zero. $m\tau j$ and $v\tau j$ are the first and second-order values of the homogenized historical gradient of ω_j, and they change with the epoch τ. β_1 and β_2 are the homogenized parameters. $\hat{Y}^{\tau-}$ is the final predicted value calculated in the (τ-1)th epoch. Y_T is the actual value.

V. ACCURACY IMPROVEMENT TECHNIQUES

The performance of deep-learning approaches relies heavily on data quality. In view of the data characteristics of OEF, the data preprocessing strategy is proposed for higher accuracy.

A. STATE FILTERING

Since the IES is usually in a reliable state without any load curtailment, the distribution of historical load curtailment is highly uneven. This is the class-imbalance problem.

Essentially, a deep learning algorithm is to obtain certain experiences from the big data. However, the accuracy is deteriorated because of the class-imbalance problem. The historical records fail to provide much information about load curtailment. Small portion load curtailment data is considered noise and ignored while training. Such data distribution can cause a greater error in the prediction of the rare curtailment.

To alleviate impediments of class imbalance, two categories (classified by whether or not load curtailment occurs) are supposed to share almost the same proportion in the training data. The raw training dataset is filtered based on the data deduplication technique to balance the two classes of state samples.

B. MINORITY OVER-SAMPLING BASED ON MCS

The size of the training dataset shrinks dramatically with data filtration. A large-scale dataset is necessary to ensure accuracy and avoid the over-fitting problem. To address this, the over-sampling strategy is proposed based on the Monte-Carlo simulation. Using the probability model of equipment

failure, more operation states are simulated in the neighboring state space by MCS and selected in the descending order of load curtailment.

C. DATA NORMALIZE TRANSFORM

Since the data scale of the different energy variables is different, it is difficult to choose a universal learning rate. The influence of key but small variables will be weak. Smaller variable fades out easily if other large variables go through the same data process. In this regard, the original data is mapped into the unit interval from 0 to 1, which can be expressed as,

$$x = \begin{cases} \dfrac{x - x_{\min}}{x_{\max} - x_{\min}}, & if\ x_{\max} - x_{\min} \neq 0 \\ x, & if\ x_{\max} - x_{\min} = 0, x_{\max} = 0 \\ \dfrac{x_{\min}}{x_{\max}}, & if\ x_{\max} - x_{\min} = 0, x_{\max} \neq 0 \end{cases} \quad (29)$$

where x is the original input. $x_{\min}$ and $x_{\max}$ are the minimal and maximal values of x. The normalized transformation for Y is in the same way with the minimal and maximal values of y.

VI. FLOWCHART OF IES RELIABILITY ASSESSMENT

The overall process of the proposed deep-learning IES reliability assessment is shown in Fig.7.

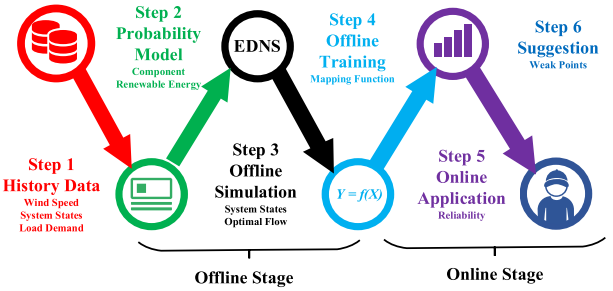

FIGURE 7. The scheme of deep-learning IES reliability assessment.

Step 1: History data collection. Experience of IES operation reflects the precise mechanism of interactions between multi-energy. In this stage, historical load demand, wind speed, solar irradiation, energy output, and energy distribution data are accumulated.

Step 2: Unavailability modeling. States of energy generation equipment, renewable energy installation, and energy conversion devices are decisive to available capacity and energy distribution. The uncertainties of equipment are simulated in MCS manners based on the two-state model. The wind speed and current solar irradiation data are randomly selected from the interpolation results according to their historical data.

Step 3: Replenish samples via simulation. Based on the probability model, the equipment states and consequent system states are simulated by MCS, and then the available capacity is determined. The optimal energy flow, load curtailment, and renewable energy loss are obtained via the interior-point algorithm and labeled as the target values.

Step 4: Network training. The deep network is trained with a Gaussian noise based on SDAE to rewrite the input features. The pre-train result is used to initialize the network parameters. Thereafter, the fully connected layer is trained with a smaller learning rate for fine-tuning.

Step 5: Online applying. Use the after-trained model to predict the optimal energy flow and minimal curtailment of load and wind energy in IES. Calculate the expected value of the predicting outcomes as the IES reliability indices.

Step 6: Reliability suggestions. The reliability indices of IES can support the analysis of weak points, and many reliability enhancement strategies are determined accordingly.

VII. CASE STUDY

The proposed deep-learning approach is tested in the IES system, as shown in Fig. 8. The WT and PV are connected to the electric bus with a converter, and the outputs of PV and WT follow their distribution of the historical data. The parameters of components are listed in Table 1. The hardware and software used in the test conditions are listed as follows: Intel i5-10600KF CPU, 16G RAM, Windows 10, and Python 3.8.

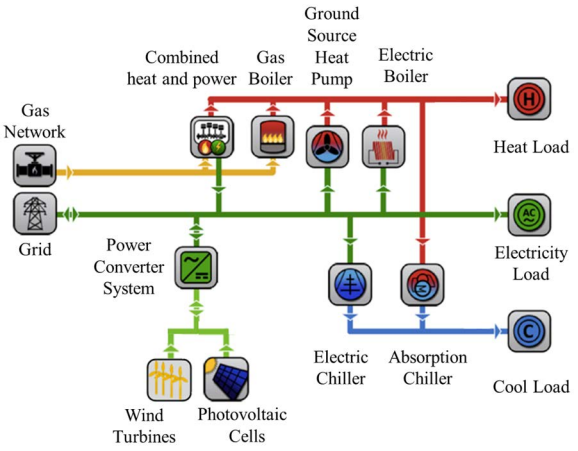

FIGURE 8. The test IES case.

TABLE 1. Parameters of components.

Equipment	U	C (kW)	f
Combined Heat and Power	0.03	5000	0.6 (heat/power)
Gas Boiler	0.025	2000	0.85
Photovoltaic Cells	0.03	1000	/
Air Source Heat Pump	0.065	2000	3
Geothermal Pump	0.065	1000	4.4
Electric Chiller	0.03	7000	3.5
Absorption Chiller	0.03	5000	0.7
Wind Turbine	0.03	1000	/
Converter	0.03	4000	

The indices used to evaluate the performance of the proposed deep-learning approach are listed as follows.

TABLE 2. Methods in details.

Methods	Description	Details			
		Stacked structure	Pre-train	Noise	State filtering
M0	Modeling method [25]				
M1	Random Forest [24]				
M2	DAE	×	×	×	×
M3	SDAE without pre-train	√	×	×	×
M4	SAE (without noise)	√	√	×	×
M5	SDAE with an imbalanced dataset	√	√	√	×
M6	SDAE with random zero noise	√	√	√	√
M7	SDAE with Gaussian Noise (the proposed method)	√	√	√	√

The absolute relative error (ARE),

$$ARE = \frac{\left|R_{real,i} - R_{pred,i}\right|}{R_{real,i}} \times 100\% \tag{30}$$

The normalized average of the squares error (NMSE),

$$NMSE = \frac{1}{N}\sum_{i=1}^{N}\frac{(R_{real,i} - R_{pred,i})^2}{R_{real,i}R_{pred,i}} \tag{31}$$

The average absolute percentage error (MAPE),

$$MAPE = \frac{1}{N}\sum_{i=1}^{N}\left|\frac{R_{real,i} - R_{pred,i}}{R_{real,i}}\right| \times 100\% \tag{32}$$

The index of agreement (IA),

$$IA = 1 - \frac{\sum_{i=1}^{N}\left(R_{pred,i} - R_{real,i}\right)^2}{\sqrt{\frac{1}{N}\sum_{i=1}^{N}R_{real,i}^2} + \sqrt{\frac{1}{N}\sum_{i=1}^{N}R_{pred,i}^2}} \tag{33}$$

The fractional bias (FB),

$$FB = \frac{2(\bar{R}_{real} - \bar{R}_{pred})}{\bar{R}_{real} + \bar{R}_{pred}} \tag{34}$$

The Theil inequality coefficient (TIC),

$$TIC = \frac{\sqrt{\frac{1}{N}\sum_{i=1}^{N}\left(R_{pred,i} - R_{real,i}\right)^2}}{\sqrt{\frac{1}{N}\sum_{i=1}^{N}R_{real,i}^2} + \sqrt{\frac{1}{N}\sum_{i=1}^{N}R_{pred,i}^2}} \tag{35}$$

where N is the number of elements in the array. R_{real} and R_{pred} denote the actual and predicted values, respectively. The error indicator reflects the numerical closeness, and FB and TIC can reflect the consistency and stability of the prediction.

A. RELIABILITY ASSESSMENT RESULTS

To demonstrate the performance of the proposed method, multiple methods in Table 2 are used in this case. M0 is the traditional MCS-based method, whose result is used as the benchmark to evaluate other data-driven methods (M1-M7). M2 and M3 are designed to analyze the effect of the stacked structure and pre-train strategy, respectively. The difference between M5 and M7 is the training dataset. M4, M6, and M7 are introduced to analyze the impact of noise settings. M7 is the proposed method. For the random mask erosion, the corruption rate is set as 0.2, while the variance of Gaussian noise is 0.05. The size of the training and validation dataset is 5740 and 20000, respectively. The neurons of each layer are set as 15, 50, 100, 200, and 14 respectively. Redundant states without load curtailment are abandoned in the state-filtering process, and 2870 items are kept (50% of the training samples). The weight homogenized parameters of the Adam optimizer are 0.7 and 0.92. The reliability results are shown in Table 4 and the comparison is analyzed in part B.

As shown in Table 4, the average accuracy of M7 in reliability assessment is 96.876%. The computing time of the proposed M7 method has been reduced by 99.99991%. The computing time is reduced by 6 orders of magnitude, which meets the requirements of online calculation.

B. PERFORMANCE ON OEF DETERMINATION

The performance indices of M1-M7 are shown in Table 3. The indices such as ARE and MAPE indicate the advantages of M7 in accuracy. In terms of FB and TIC, M7 shows a lower dispersion degree and better data consistency.

Calculated from the average MAE, the proposed method M7 in OEF accuracy is 96.57% as compared to M1 and M2 with accuracy rates of 18.50% and 90.39% respectively. The results of M1 show the random forest method is not comparable with the SDAE method. M2 indicates that the stacked structure and deep learning algorithm help improve accuracy by offering more types of feature interaction.

Comparing M3 with M7, pre-training improves the effects of feature extraction. Compared with M5, the proposed pre-filtering strategy improves the accuracy by enriching the minority samples.

Results of M4, M6, and M7 prove the effectiveness of the Gaussian noise strategy. The results show that OEF accuracy of for M7 is 95.86% as compared to 90.32% and 88.55% for M4 and M6 respectively. M6 has the worst prediction because the input features are polluted by the random zero and the network is trained based on insufficient information. Compared with M4 and M7, the proposed noise erosion strategy further improves the accuracy because the Gaussian noise

TABLE 3. Performance indices for comparison.

Performance Indices	M1	M2	M3	M4	M5	M6	**M7**
Average ARE	0.8150	0.0961	0.0968	0.1145	0.1004	0.0874	**0.0660**
Max ARE	3.6082	0.3180	0.3232	0.2869	0.3420	0.1746	**0.1565**
NMSE	0.4251	0.0122	0.0124	0.0146	0.0139	0.0081	**0.0057**
MAPE	0.6155	0.0802	0.0806	0.1022	0.0832	0.0812	**0.0639**
IA	0.9999	0.9999	0.9999	0.9999	0.9999	0.9998	**0.9999**
FB	0.0016	-0.0041	-0.0141	-0.0228	-0.0241	-0.0326	**-0.0034**
TIC	0.0108	0.0122	0.0095	0.0091	0.0096	0.0133	**0.0097**

TABLE 4. IES reliability assessment results.

Case	Time (s)	EDNS (kW)			Loss (kW)	
		Power	Heat	Cool	PV	Wind
M0	58520.033	15.307	20.784	191.018	6.183	7.523
M7	0.054	14.974	22.172	200.320	6.414	7.826

increases the similarity between the training dataset and the real data. Furthermore, the proposed Gaussian noise strategy also enriches the training samples and improves generalization capabilities.

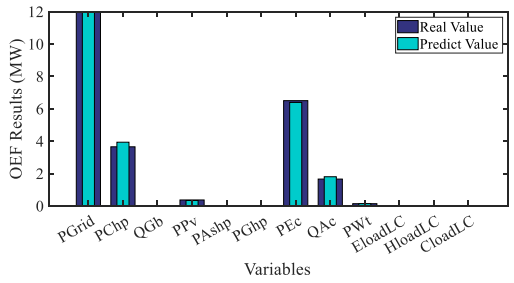

FIGURE 9. The OEF results at 17:00 in summer.

Apart from the curtailment prediction, the proposed method can be used to predict OEF operation strategies in different scenarios. Fig.9 shows the operating results for IES without failure, and Fig.10 shows the operating results of IES when the AC is out of service.

Since AC absorbs heat and converts it into cooling energy, the outage of AC results in a cooling shortage in summer. On the other hand, the heat cannot be consumed by AC leading to the reduction of CHP output. Consequently, the power generation is decreased and the power consumption of EC is limited. The shortage of cooling output is intensified and eventually causes the high cooling curtailment. Compared with the real value, the predicted results of OEF are quite accurate for these two different scenarios. The proposed method is proved to accommodate the complex changes described above.

C. GAUSSIAN NOISE STRATEGY FOR IES DATA

Gaussian noise can enrich the training data by varying the data partially. The prediction accuracy is related to the noise

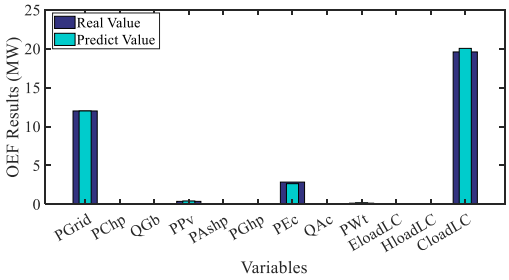

FIGURE 10. The OEF results at 17:00 in summer with AC outage.

strategy. The failure of the random mask strategy indicates that large distortion of the input features should be avoided. The variance of Gaussian noise is an important factor in the transformation.

Fig.11 shows an ideal variance is around 0.02. Fig.12 shows the reason is the lower relative error and degree of variation. The noise can help to overcome the overfitting problem of training and avoid great discrepancy. As shown in Fig.12, the higher variance is detrimental to network training. From aspects of FB and TIC, higher variance results in lower agreement and prediction consistency.

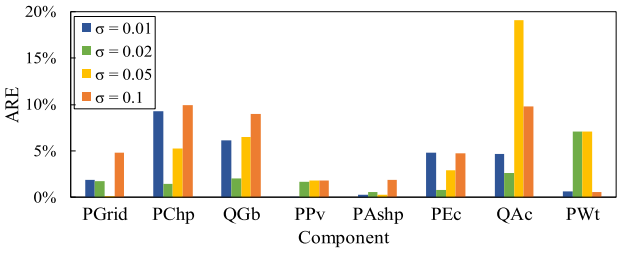

FIGURE 11. Influence of noise variances on OEF results.

D. SYSTEM WEAKNESS ANALYSIS

The proposed model can be used to analyze the reliability indices of components, as shown in Table 5 and Fig. 13. The EC and AC are the weak points of IES. Their outages can pose the most severe threat to the cooling supply. The ASHP and GHP are critical to the heat supply. In addition, weak points can be identified within 1 second with the proposed method.

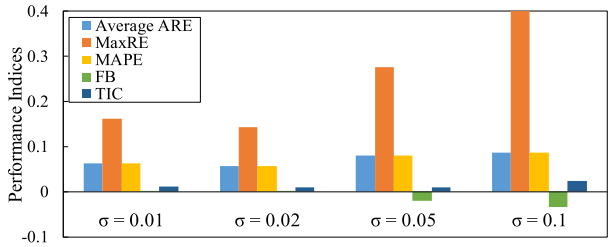

FIGURE 12. Influence of noise variances on performance indices.

TABLE 5. Reliability indices of IES components.

Components	EDNS (kW)			Time (s)
	Power	Heat	Cool	
CHP	13.3379	2.1630	6.5422	0.05157
GB	0.4327	1.4499	6.1792	0.05194
ASHP	0.7260	1.1696	6.7293	0.05166
GHP	1.0628	22.3858	14.6508	0.05155
EC	1.0640	10.4403	14.7150	0.05154
AC	0.0004	1.1716	124.9388	0.05152
PV	0.0006	1.1692	76.3751	0.05154
WT	0.4734	1.1692	6.5411	0.05149
PCS	1.0263	1.1696	7.0527	0.05157

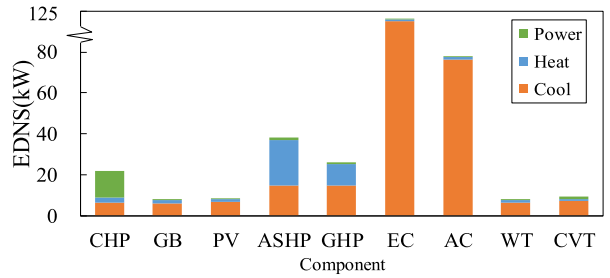

FIGURE 13. The reliability indices of components in IES.

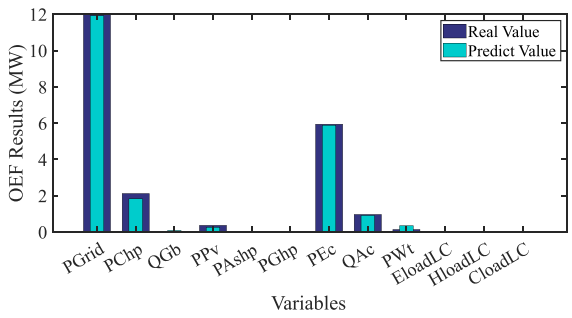

FIGURE 14. The OEF result with 90% of load.

E. SCENARIO ROBUSTNESS

To demonstrate the scenario robustness of the proposed method, the cases of IES with 90% and 110% of load are tested. Fig.14 is a typical summer day and the IES operates at the 90% load level. In Fig.15, PV is out of service on a spring day and the IES operates at 110% of load levels. The OEF accuracy of Fig.14 and 15 are 90.02% and 94.25%. The

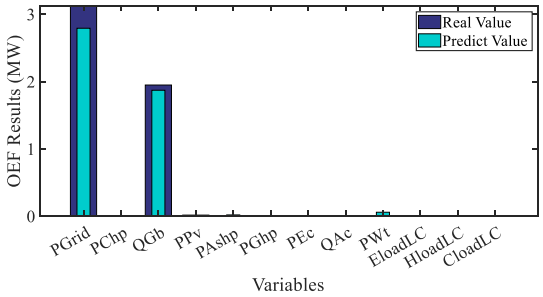

FIGURE 15. The OEF result with 110% of load and PV outage.

proposed method can provide an energy allocation strategy for different scenarios. with over 90% accuracy from a numerical standpoint.

VIII. CONCLUSION

This paper proposes an SDAE-based method to determine the optimal energy flow in IES and offers an efficient way to assess the reliability. The proposed method can accelerate IES reliability assessment by 6 orders of magnitude. The results demonstrated that the SDAE-based method has good performance with an accuracy of 96.57% as compared to RF and DAE with accuracy rates of 18.50% and 90.39% respectively. The proposed method improves the accuracy from 88.55% by replacing the random-zero noise with Gaussian noise. The results also show that the accuracy of strategy for OEF prediction is over 90% with different load levels. Based on these results it can be concluded that the proposed scheme provides high accuracy and scenario robustness. With the proposed reliability scheme, IES weakness can be identified for no more than 1 second. Because labeling samples is a costly work, the future work is to study an algorithm that can learn on unlabeled data.

REFERENCES

[1] G. Li, Z. Bie, Y. Kou, J. Jiang, and M. Bettinelli, "Reliability evaluation of integrated energy systems based on smart agent communication," *Appl. Energy*, vol. 167, pp. 397–406, Apr. 2016.

[2] Office of Cybersecurity, Energy Security, and Emergency Response. *Extreme Cold & Winter Weather*. Accessed: Feb. 16, 2021. [Online]. Available: https://www.energy.gov/ceser/downloads/extreme-coldwinter-weather-hub-situation-update-1

[3] H. Zhu. *2021 Texas Power Outages: Facts and Initial Thoughts*. Accessed: Feb. 22, 2021. [Online]. Available: http://sites.utexas.edu/ haozhu/

[4] D. Lenton. *National Grid Blackout Report Fails to Get to Heart of Problems*. Accessed: Aug. 21, 2019. [Online]. Available: https://eandt.theiet.org/content/articles/2019/08/national-grid-blackout-report-fails-to-get-toheart-of-problems/

[5] H.-H. Yu, K.-H. Chang, H.-W. Hsu, and R. Cuckler, "A Monte Carlo simulation-based decision support system for reliability analysis of Taiwan's power system: Framework and empirical study," *Energy*, vol. 178, pp. 252–262, Jul. 2019.

[6] Y. Tang, Y. Zhao, W. Li, K. Xie, and J. Yu, "Incorporating compressor station multiple failure modes in risk evaluation of electricity-gas integrated energy systems," *CSEE J. Power Energy*, early access, Jun. 25, 2021. [Online]. Available: https://ieeexplore.ieee.org/document/9465784, doi: 10.17775/CSEEJPES.2020.05850.

[7] M. Bao, Y. Ding, C. Shao, Y. Yang, and P. Wang, "Nodal reliability evaluation of interdependent gas and power systems considering cascading effects," *IEEE Trans. Smart Grid*, vol. 11, no. 5, pp. 4090–4104, Sep. 2020.

[8] C. M. Correa-Posada and P. Sánchez-Martín, "Integrated power and natural gas model for energy adequacy in short-term operation," *IEEE Trans. Power Syst.*, vol. 30, no. 6, pp. 3347–3355, Nov. 2015.
[9] S. Bao, Z. Yang, J. Yu, W. Dai, L. Guo, and H. Yu, "Probabilistic energy flow and risk assessment of electricity–gas systems considering the thermodynamic process," *Energy*, vol. 189, Dec. 2019, Art. no. 116263.
[10] A. Zhang, G. Peng, W. Yang, G. Qu, and H. Huang, "Risk assessment of offshore micro integrated energy system based on fluid mosaic model," *IEEE Access*, vol. 8, pp. 76715–76725, 2020.
[11] S. Zhang, W. Gu, S. Yao, S. Lu, S. Zhou, and Z. Wu, "Partitional decoupling method for fast calculation of energy flow in a large-scale heat and electricity integrated energy system," *IEEE Trans. Sustain. Energy*, vol. 12, no. 1, pp. 501–513, Jan. 2021.
[12] J. Yu, L. Guo, M. Ma, S. Kamel, W. Li, and X. Song, "Risk assessment of integrated electrical, natural gas and district heating systems considering solar thermal CHP plants and electric boilers," *Int. J. Electr. Power Energy Syst.*, vol. 103, pp. 277–287, Dec. 2018.
[13] M. Cao, C. Shao, B. Hu, K. Xie, W. Li, L. Peng, and W. Zhang, "Reliability assessment of integrated energy systems considering emergency dispatch based on dynamic optimal energy flow," *IEEE Trans. Sustain. Energy*, vol. 13, no. 1, pp. 290–301, Jan. 2022.
[14] H. W. Dommel and W. F. Tinney, "Optimal power flow solutions," *IEEE Trans. Power App. Syst.*, vol. PAS-87, no. 10, pp. 1866–1876, Oct. 1968.
[15] Z. Xu, G. Han, L. Liu, M. Martínez-García, and Z. Wang, "Multi-energy scheduling of an industrial integrated energy system by reinforcement learning-based differential evolution," *IEEE Trans. Green Commun. Netw.*, vol. 5, no. 3, pp. 1077–1090, Sep. 2021.
[16] N. Liu, J. Wang, and L. Wang, "Hybrid energy sharing for multiple microgrids in an integrated heat-electricity energy system," *IEEE Trans. Sustain. Energy*, vol. 10, no. 3, pp. 1139–1151, Jul. 2019.
[17] B. Miao, J. Lin, H. Li, C. Liu, B. Li, X. Zhu, and J. Yang, "Day-ahead energy trading strategy of regional integrated energy system considering energy cascade utilization," *IEEE Access*, vol. 8, pp. 138021–138035, 2020.
[18] N. Liu, L. Tan, H. Sun, Z. Zhou, and B. Guo, "Bilevel heat–electricity energy sharing for integrated energy systems with energy hubs and prosumers," *IEEE Trans. Ind. Informat.*, vol. 18, no. 6, pp. 3754–3765, Jun. 2022.
[19] Z. Liu, K. Hou, H. Jia, J. Zhao, D. Wang, Y. Mu, and L. Zhu, "A Lagrange multiplier based state enumeration reliability assessment for power systems with multiple types of loads and renewable generations," *IEEE Trans. Power Syst.*, vol. 36, no. 4, pp. 3260–3270, Jul. 2021.
[20] C. Wang, C. Yan, G. Li, S. Liu, and Z. Bie, "Risk assessment of integrated electricity and heat system with independent energy operators based on Stackelberg game," *Energy*, vol. 198, May 2020, Art. no. 117349.
[21] S. A. Vaghefi, M. A. Jafari, J. Zhu, J. Brouwer, and Y. Lu, "A hybrid physics-based and data driven approach to optimal control of building cooling/heating systems," *IEEE Trans. Autom. Sci. Eng.*, vol. 13, no. 2, pp. 600–610, Apr. 2016.
[22] A. T. Eseye and M. Lehtonen, "Short-term forecasting of heat demand of buildings for efficient and optimal energy management based on integrated machine learning models," *IEEE Trans. Ind. Informat.*, vol. 16, no. 12, pp. 7743–7755, Dec. 2020.
[23] X. Su, X. Bai, Y. Zheng, S. Wei, and Z. Qin, "Data-driven robust dispatch of integrated electricity-gas energy systems considering uncertainty of wind power," in *Proc. IEEE PESGM*, Atlanta, GA, USA, Aug. 2019, pp. 4–8.
[24] B. Zhang, M. Wang, and W. Su, "Reliability analysis of power systems integrated with high-penetration of power converters," *IEEE Trans. Power Syst.*, vol. 36, no. 3, pp. 1998–2009, May 2021.
[25] H. Zhang, P. Wang, S. Yao, X. Liu, and T. Zhao, "Resilience assessment of interdependent energy systems under hurricanes," *IEEE Trans. Power Syst.*, vol. 35, no. 5, pp. 3682–3694, Sep. 2020.
[26] Z. Zeng, T. Ding, Y. Xu, Y. Yang, and Z. Dong, "Reliability evaluation for integrated power-gas systems with power-to-gas and gas storages," *IEEE Trans. Power Syst.*, vol. 35, no. 1, pp. 571–583, Jan. 2020.
[27] Z. Dong, K. Hou, H. Meng, X. Yu, and H. Jia, "Data-driven power system reliability evaluation based on stacked denoising auto-encoders," *Energy Rep.*, vol. 8, pp. 920–927, Apr. 2022.

ZIHENG DONG received the B.S. degree in electrical engineering from Tianjin University, Tianjin, China, in 2020, where she is currently pursuing the M.S. degree with the Electrical Engineering Department. Her research interests include reliability and risk assessment of power systems and data-driven methods for power systems.

KAI HOU (Member, IEEE) received the Ph.D. degree in electrical engineering from Tianjin University, Tianjin, China, in 2016. He is currently an Associate Professor with the Electrical Engineering Department, Tianjin University. His research interests include reliability and risk assessments of power systems, integrated energy systems, and smart grids.

ZEYU LIU (Student Member, IEEE) received the B.S. degree from Tianjin University, Tianjin, China, in 2018, where he is currently pursuing the Ph.D. degree with the School of Electrical and Information Engineering, Tianjin University. His research interests include power system reliability assessment, uncertainty analysis, and integrated energy systems planning and reliability evaluation.

XIAODAN YU received the B.S. and M.S. degrees in electrical engineering from Tianjin University, Tianjin, China, in 1996 and 1999, respectively. She is currently an Associate Professor with the Electrical Engineering Department, Tianjin University. Her research interests include power reliability assessment, stability analysis, distribution network planning and automation, and integrated energy systems.

HONGJIE JIA (Senior Member, IEEE) received the B.S., M.S., and Ph.D. degrees in electrical engineering from Tianjin University, Tianjin, China, in 1996, 1999, and 2001, respectively. He is currently a Professor with the Electrical Engineering Department, Tianjin University. His research interests include power reliability assessment, stability analysis and control, distribution network planning and automation, and integrated energy systems.

QIAN XIAO (Member, IEEE) received the Ph.D. degree in electrical engineering from Tianjin University, Tianjin, China, in 2020. He is currently an Associate Professor with the Electrical Engineering Department, Tianjin University. His research interests include distributed energy and microgrids, artificial intelligence in power systems, and power electronics technology.